Available online at www.sciencedirect.com
SCIENCE DIRECT®
Sensors and Actuators A 121 (2005) 35–43
SENSORS AND ACTUATORS A PHYSICAL
www.elsevier.com/locate/sna

Wireless bimorph micro-actuators by pulsed laser heating

Li-Hsin Han, Shaochen Chen*

Department of Mechanical Engineering, The University of Texas at Austin, 1 University Station, C2200, Austin, TX 78712, USA

Received 19 August 2004; received in revised form 28 November 2004; accepted 11 December 2004
Available online 19 January 2005

Abstract

We report an experimental and theoretical investigation on wireless bimorph micro-cantilever (BMC) actuated by pulsed laser heating. The micromachined BMC consists of a thin gold layer deposited on a polysilicon layer. A pulsed Nd:YAG laser of wavelength = 355 nm and pulse width = 12 ns was used to heat the BMC. The movement of the BMC was measured by a displacement sensor. Experimental results revealed the frequency of BMC vibration upon laser heating. A two-dimensional (2D) discrete model was developed to simulate the laser pulse response of the cantilever. The simulation results agreed well with experimental observation, except the minor differences in vibration amplitudes in the model.

Keywords: Laser; Micro-cantilever; MEMS; Model; Wavelength; Pulse

1. Introduction

The use of bimorph micro-cantilevers (BMC) has become a fundamental technology in the field of micro-electro-mechanical systems (MEMS). In a microsystem, a BMC is usually used to convert the energy from a specific power source to a mechanical force, which produces bending moments and structural deformation. Mechanisms to produce the mechanical force include material phase-change, capacitive-electrical force, and thermal expansion [1–3]. Despite the wide variety of the deformation mechanisms, most of the BMCs are electrically powered. Such micro-systems require wiring, which may limit their use due to device packaging difficulties, a conductive environment, or an enlarged device size.

A possible solution for wireless actuation is to use a laser as the power source to heat the BMC. This concept has been demonstrated in laser-heated micro-cantilevers for biological detection [4]. A continuous-wave (CW) laser was applied to successfully heat and bias the position of the bimorph micro-cantilevers in water. BMCs were also used to develop photo-detectors where a BMC- or BMC-array could be employed to interact with the energy from an infrared source [5,6]. BMC deformation was used to characterize the intensity or intensity distribution of the infrared sources. Moreover, a CW laser beam has been applied in actuating micro-mirrors and a micro-cantilever [7,8].

When using a laser to actuate a BMC the deformation of the BMC is related to the absorption rate of the laser energy and the heat dissipation rate in the BMC. The difference between these two rates decides how much thermal energy the BMC will contain and what temperature the BMC will have, which determines the amount of deformation the BMC can generate. If a large deformation is desired, one has to either raise the intensity of the CW laser or reduce the thermal conductivity of the BMC by changing the materials of the BMC. In some applications of laser heating, such as micro-pumping or micro-propelling, it is more preferable to create a pulse-like deformation rather than a smooth deformation in the microstructure. A pulsed laser is an effective tool to provide the energy for the pulse-like deformations. For example, a nanosecond-pulsed laser can deposit its energy to a microstructure within nanoseconds, before a substantial amount of heat is dissipated, and result in a very high temperature within the microstructure [9].

* Corresponding author. Tel.: +1 512 2326094; fax: +1 512 4711045.
E-mail address: scchen@mail.utexas.edu (S. Chen).

0924-4247/$ – see front matter © 2004 Elsevier B.V. All rights reserved.
doi:10.1016/j.sna.2004.12.012

The sudden increase in the temperature of the microstructure usually generates structural vibrations, which are a result of thermal expansion. These effects have been reported in sound generation in high-power laser-heated gas particles [10]. These vibrations in microstructures are promising for the application of micro-pumping or micro-propelling.

In this article, we report the experimental and theoretical investigation of pulsed-laser interaction with BMCs that have a gold layer on a polysilicon (poly-Si) layer. A Nd:YAG laser of wavelength of 355 nm and pulse width of 12 ns was used to heat the BMC. The bending of the BMC was optically measured with a displacement detector. To better understand the experimental observation, a 2D discrete model was developed to simulate the motion of the BMC induced by pulsed laser heating. Numerical results were compared with the experimental results to reveal the physical mechanisms of laser-BMC actuation.

2. Experiments

The design of the BMCs is shown in Fig. 1. The structure was designed by a Poly-MUMPS® process provided by MEMSCAP. The BMCs are on a silicon substrate coated with a 600 nm silicon nitride layer. The length of the BMCs are 1000, 850, and 500 μm, respectively. The bilayer structure is made of a 1.5 μm thick poly-Si layer and a 0.5 μm thick Au layer. It was discovered that the cantilever bended upward because of the internal stress between the two layers (Fig. 2) after release by using buffered

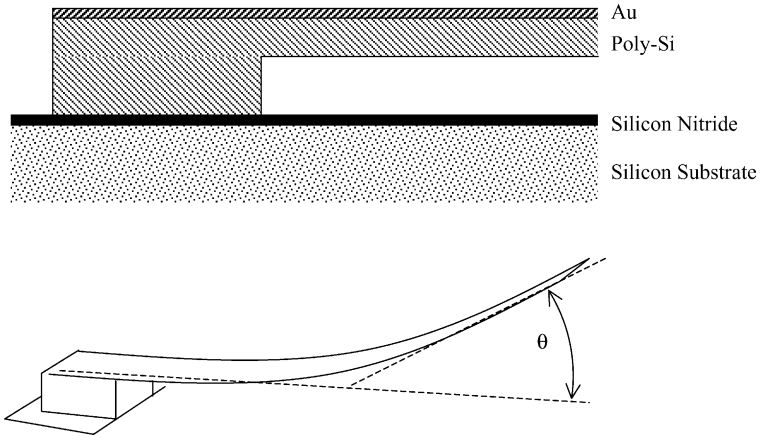

Fig. 1. A schematic diagram of a BMC.

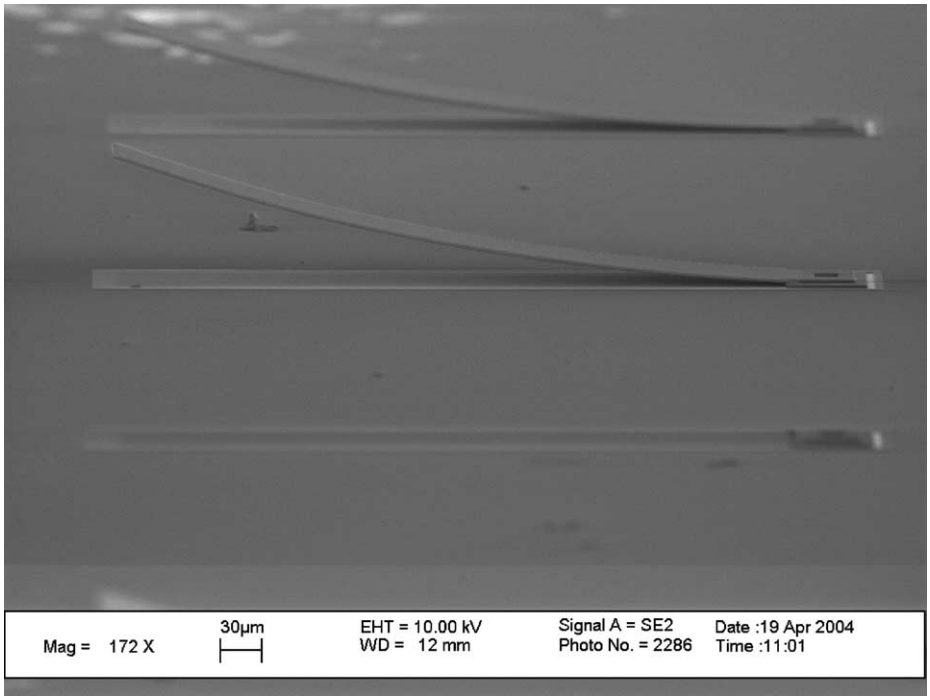

Fig. 2. An SEM image of the BMCs with initial bending.

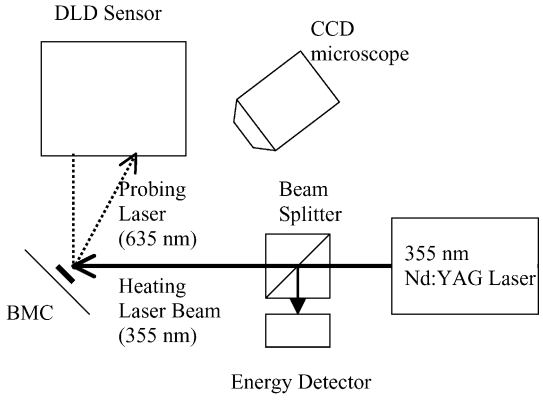

Fig. 3. An experimental setup for measuring laser-actuated BMC motion. The 355 nm Nd:YAG laser is for BMC actuation, while the 635 nm diode laser is for displacement detection.

hydro-fluoride acid (BHF). The internal stress was a result of different thermal expansion coefficients of the poly-Si and Au layers. The initial bending angle θ of 1000, 850, and 500 μm BMCs were approximately 23°, 20°, and 12°.

The experimental setup of a laser-actuated BMC is shown in Fig. 3. A laser pulse from a Nd:YAG laser ("heating laser", wavelength = 355 nm, pulse width = 12 ns) was delivered to the top gold layer to heat the BMCs. A beam splitter was used to deliver a portion of the laser to an energy detector to measure the laser power. To detect the movement of the BMC, a commercial diode laser displacement sensor (DLD sensor, MICROTRAK®) was used. The DLD sensor included a diode laser (CW) of wavelength at 635 nm and a position-sensitive diode (PSD) module. The diode laser ("probing laser") probed the BMC that was heated by the Nd:YAG laser. The reflected probing laser beam was collected by the PSD module. The PSD module has a position-sensitive diode, which is sensitive to the projected location of the reflected probing laser beam. When the sample (cantilever) surface moves, the reflected laser spot moves and the resistance of the PSD changes. A central unit of the DLD sensor analyzes the variation of the PSD resistance and calculates the distance from the BMC surface to the PSD. To optimize the detecting signal, the angle between the surface gold layer and the DLD sensor, β (Fig. 4), was set to 40°, the angle at which most of the incident energy of the diode laser could be reflected to the PSD.

The DLD sensor has a port that output a voltage proportional to the distance measured. The range of the output voltage is ±5 V, corresponding to the range of the DLD sensor, ±1.25 mm. We used an oscilloscope with a 500 MHz bandwidth and a 1 GSa/s sampling rate operated on single-shot acquisition mode (1 ns time resolution) to receive the voltage and to generate a displacement waveform in real time. A CCD-coupled microscope was used to monitor the laser spots to ensure that both the heating laser and the probing laser spots were targeted on the BMC.

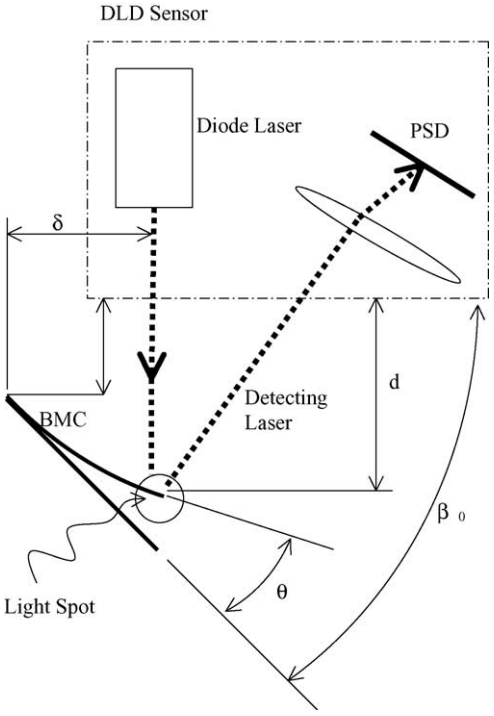

Fig. 4. Components of the diode laser displacement sensor system (DLD). It detects the distance d in real time. θ is the bending angle of the BMC and δ the horizontal distance from the BMC base to the light spot. The angle β was about 40° at which most of the energy from the laser spot could be reflected to the PSD module. These values have also been used for the simulation of BMC vibration.

3. Simulation

The goal of this simulation is to reveal the mechanism of thermal-induced-bending of the laser-actuated BMC. Both dynamics issues and heat transfer issues are considered in the simulation. Table 1 lists the variables used in modeling.

3.1. Dynamics model

We developed a discrete 2D model to simulate the dynamics of the BMC. The cantilever was simulated with N identical rigid rods connected in series by rotary linkages. Each of the rotary linkages has a torsional spring with spring constant K_{elastic}. The first of the rods connects to a fixed wall by one of the rotary linkages, so that a clamp-free cantilever model is formed. The coordinate system of the model is an X–Y-axis system. Each of the rods has mass m_{rod}, mass moment of inertia I_{rod}, and length l. K_{elastic} is derived from the theoretical reactive-torque of a bimorph cantilever beam under a bending curvature ζ [11]:

$$\tau = \frac{E_1 I_{1c} + E_2 I_{2c}}{\zeta} \quad (1)$$

I_{1c} and I_{2c} are moments of inertia of the two layers with respect to the centroidal axis of the beam's cross-section: $I_{ic} = I_{i0} + A_i d_i^2$, $I_{i0} = b a_i^3/12$, $A_i = b a_i$,

Table 1
The variables in the BMC model

Variable	Description	Given value	Unit
a_1, a_2	Thickness of the first (silicon) and second (gold) layers	1.5 and 0.5	μm
b	BMC width	60	μm
E_1, E_2	Young's modules of materials of the first and second layers	122.4 and 77.2	GPa
α_1, α_2	Thermal expansion coefficients of the materials of the first and second layers	3.2E−6 and 14.5E−6	K^{-1}
L	BMC beam length	500, 850, and 1000	μm
ρ_1, ρ_2	Material densities of the first and second layers	2328 and 19320	kg/m^3
ρ_a	Air density	1.225	kg/m^3
C_{V1}, C_{V2}	Specific heat of the first and second layers	702.0 and 132.3	J/K kg
k_1, k_1	Thermal conductivities of the first and second layers	124.0 and 301.0	W/m K
R	Reflectivity of the top layer surface (gold) against incident 355 nm laser	0.2	–
D	Laser beam diameter	1.0	mm
t_w	Laser pulse width	12	ns
N	Number of rods in the rods-and-linkages model	–	–
θ_{equi}	Equilibrium bending angle at temperature T	Calculated from given values	rad
θ_k	Tilting angle of the rod k in the rods-and-linkages model	Calculated from given values	rad
I_1, I_2 ($I_{1,2} = ba_{1,2}^3/12$)	Area moment of inertias of the cross-section of the first and second layers relative to their own centroidal axis (parallel to the Z-axis in our model)	Calculated from given values	m^4
I_{1c}, I_{2c}	Area moment of inertias of the cross-section of the first and second layers relative to the centroidal axis (parallel to the Z-axis in our model) of the cross-section's of the whole beam	Calculated from given values	m^4
ΔT	Temperature change from an original temperature	Calculated from given values	K
l (=L/N)	Length of each rod in the rods-and-linkages model	Calculated from given values	μm
m_{rod} (=$lb(a_1\rho_1 + a_2\rho_2)$)	The mass of each rod k in the rods-and-linkages model	Calculated from given values	kg
I_{rod} (=$m_{rod}l^2/12$)	Mass moment of inertias of each rod relative to its centroidal axis (parallel to the Z-axis in our model)	Calculated from given values	kg m^2

$d_1 = (E_2a_2^2 + E_2a_1a_2)/(E_1a_1 + E_2a_2)$, and $d_2 = (E_1a_1^2 + E_1a_1a_2)/(E_1a_1 + E_2a_2)$. Since the length of each section of the model is l, from (1) we have

$$K_{\text{elastic}} = \frac{E_1I_{1c} + E_2I_{2c}}{l} \tag{2}$$

We generated the dynamics equations of the rods-and-linkages model by Lagrange formula [12,13]. Firstly, the position of the center of each rod $\vec{P}_k$ was represented by

$$\vec{P}_k = \left(\frac{l}{2}\cos\theta_k + \sum_{i=1}^{k-1} l\cos\theta_i\right)\hat{x} + \left(\frac{l}{2}\sin\theta_k + \sum_{i=1}^{k-1} l\sin\theta_i\right)\hat{y} \tag{3}$$

the kinetic co-energy [13] of the rod T_k is

$$T_k = \tfrac{1}{2}m_{\text{rod}}|\dot{\vec{P}}|^2 + \tfrac{1}{2}I_{\text{rod}}(\dot{\theta}_k)^2 \tag{4}$$

Eqs. (3) and (4) will lead to the kinetic co-energy of the whole system as

$$T = \sum_{k=1}^{N} T_k \tag{5}$$

The potential energy of the system is

$$V = \sum_{i=2}^{N} \frac{1}{2}K_{\text{elastic}}(\theta_i - \theta_{i-1})^2 \tag{6}$$

and the Lagrangian of the system is

$$L = T - V \tag{7}$$

3.1.1. Model of free vibration

When there is no external force, i.e., bending moments or damping, the dynamics equation for the cantilever system is [12]

$$\frac{\mathrm{d}}{\mathrm{d}t}\left(\frac{\partial L}{\partial \dot{\theta}_k}\right) - \frac{\partial L}{\partial \theta_k} = 0, \quad k = 1, 2, 3, \ldots, N \tag{8}$$

According to (8), we derived the dynamics equations in matrix form

$$\begin{bmatrix} A_{1,1} & A_{1,2} & \cdots & A_{1,N} \\ A_{2,1} & A_{2,2} & & \vdots \\ \vdots & & \ddots & \vdots \\ A_{N,1} & \cdots & \cdots & A_{N,N} \end{bmatrix} \begin{bmatrix} \ddot{\theta}_1 \\ \ddot{\theta}_2 \\ \vdots \\ \ddot{\theta}_N \end{bmatrix} = \begin{bmatrix} B_1 \\ B_2 \\ \vdots \\ B_N \end{bmatrix} \quad \text{or}$$

$$\tilde{A}(\Theta, \dot{\Theta})\ddot{\Theta} = \tilde{B}(\Theta, \dot{\Theta}) \tag{9}$$

where $A_{i,j} = A_{i,j}(\theta_1, \ldots, \theta_N, \dot{\theta}_1, \ldots, \dot{\theta}_N)$ and $B_i = B_i(\theta_1, \ldots, \theta_N, \dot{\theta}_1, \ldots, \dot{\theta}_N)$.

We used MATLAB® to simulate the free vibration of the BMC of 500 μm long. In the simulation, the BMC was initially stationary and was under a uniform bending moment parallel to the Z direction. The bending moment provided each of the elastic linkages an identical bending angle. At $t = 0$, the bending was released and the system began to experience a free vibration. We studied the simulation results with different linkage numbers (N). Fast Fourier transform (FFT) [14] was used to analyze the time-domain results (Fig. 5), such that the natural frequencies of the model were revealed (Fig. 6). The time of the simulation was set to be 10.6 μs,

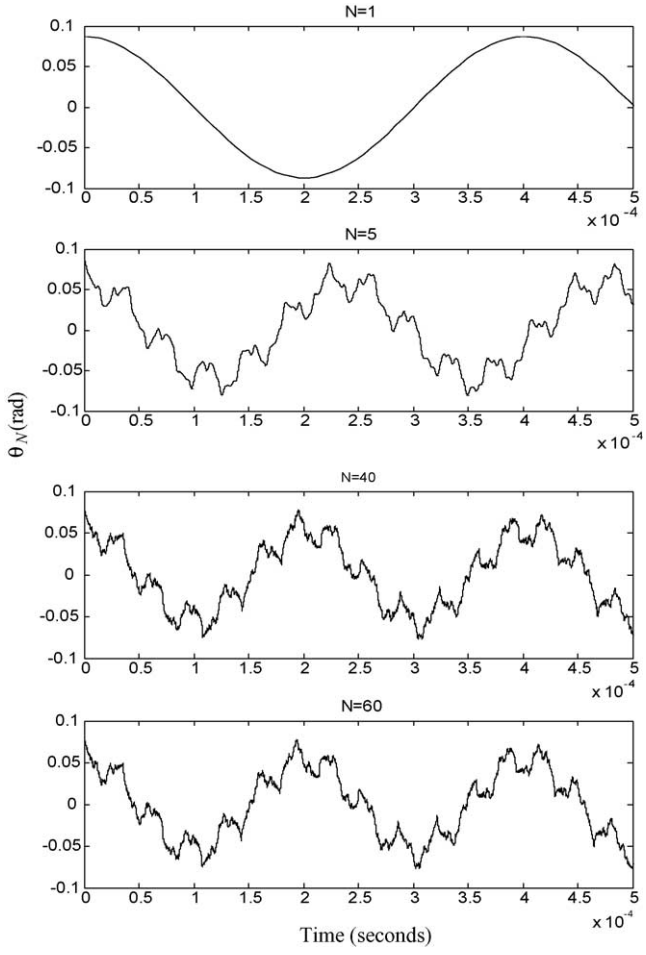

Fig. 5. The time-domain simulation result with respect to the models having different number of rods (N). The curves show the vibration of θ_N, tilting angle of the last rod that forms the free-end of the cantilever.

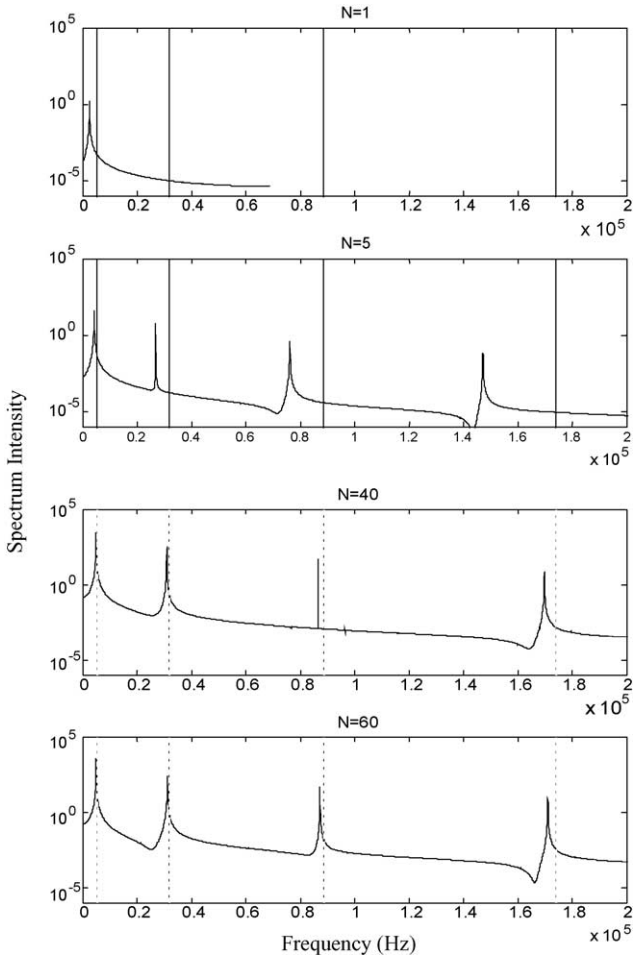

Fig. 6. The FFT frequency spectrum of the simulation results of models having different number of rods (N). The dotted lines indicate the theoretical natural frequencies of the first four orders derived by Bernoulli–Euler beam theory. These theoretical frequencies are: 5.06, 31.69, 88.73, and 173.88 kHz.

which was long enough for us to achieve a FFT frequency resolution of 100 Hz.

We compared the results from the FFT analysis and those from theoretical calculation. According to the Bernoulli–Euler beam theory [15], a clamped–free bi-layered beam has natural frequencies of

$$f_n = \frac{\lambda_n^2}{2\pi L^2}\sqrt{\frac{E_1 I_{1c} + E_2 I_{2c}}{A_1\rho_1 + A_2\rho_2}}, \quad n = 1, 2, 3, \ldots \tag{10}$$

where $A_{1,2}$ and $\rho_{1,2}$ are the cross-sectional areas and the densities of the two layers, respectively. L is the length of the beam. Each eigenvalue λ_n satisfies the condition of $\cos\lambda_n \cosh\lambda_n = -1$ [15].

In Fig. 6, we used dotted lines to mark the first four orders of theoretical natural frequencies derived from (10). It shows that, as N increases, the number of FFT peaks (indicating the natural frequencies) increases and the peaks gradually converge to the theoretical values.

To evaluate the accuracy of the model, we converted simulated natural frequencies $f_{n,\mathrm{sim}}$ into the squares of simulated eigenvalues $\lambda_{n,\mathrm{sim}}^2$:

$$\lambda_{n,\mathrm{sim}}^2 = 2\pi L^2 f_{n,\mathrm{sim}}\sqrt{\frac{A_1\rho_1 + A_2\rho_2}{E_1 I_{1c} + E_2 I_{2c}}}, \quad n = 1, 2, 3, \ldots \tag{11}$$

In Fig. 7, we used $\lambda_{n,\mathrm{sim}}^2/\lambda_{n,\mathrm{theory}}^2$ to calculate the accuracy of $\lambda_{n,\mathrm{sim}}^2$. It shows that the precision of the first four $\lambda_{n,\mathrm{sim}}^2/\lambda_{n,\mathrm{theory}}^2$ became larger than 95% when N is over 20. Since f is proportional to λ_n^2 and λ_n is non-dimensional, we know that by using the rod- and linkage model, the accuracy of the first four simulated natural frequencies can exceed 95% when the rod number N is over 20.

3.1.2. The effect of thermal bending moment

When there are external forces, the dynamics equation for the cantilever system becomes [12]

$$\frac{\mathrm{d}}{\mathrm{d}t}\left(\frac{\partial L}{\partial \dot{\theta}_k}\right) - \frac{\partial L}{\partial \theta_k} = \sum_i \vec{F}_i \frac{\partial(\vec{q}_i)}{\partial \theta_k}, \quad k = 1, 2, 3, \ldots, N \tag{12}$$

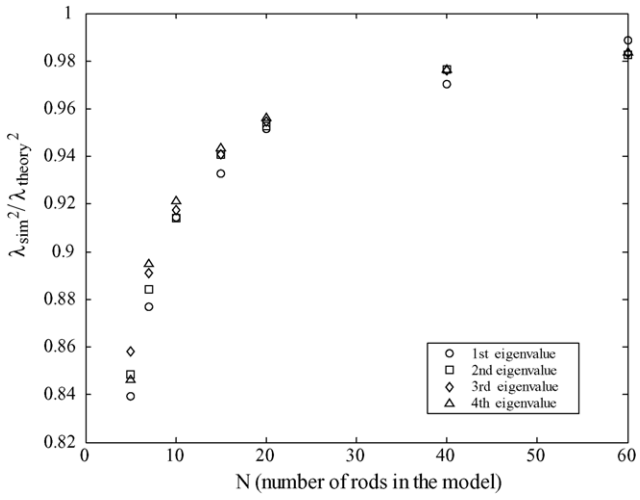

Fig. 7. The values of $\lambda_{n,\mathrm{sim}}^2/\lambda_{n,\mathrm{theory}}^2$ with respect to the models having different number of rods (N). These values also indicate the precision of the first four simulated natural frequencies with respect to the theoretical values. The symbols distinguish the $\lambda_{n,\mathrm{sim}}$'s and $\lambda_{n,\mathrm{theory}}$'s of the first four different vibration orders (circle: first order, square: second order, diamond: third order, and triangle: fourth order).

where $\vec{F}_i$ represents a non-conservative force [12] and $\vec{q}_i$ is the displacement of the point at which the force is applied.

Let us first discuss the effect of thermal bending. Assuming that there is a thin bimorph cantilever, and it was initially straight. When the local temperature in a position of the cantilever is raised by ΔT, the thin bimorph cantilever would be bended locally at that position by a bending curvature ζ [16]:

$$\frac{1}{\zeta} = \frac{\alpha_2 - \alpha_1}{(E_1/a_2 + E_2/a_1)[2(E_1I_1 + E_2I_2)/(a_1 + a_2) + (a_1 + a_2)/2(1/a_1E_1 + 1/a_2E_2)] \times \Delta T} = C\,\Delta T \tag{13}$$

where C is a constant. The α_1 and α_2 are the thermal expansion coefficients of the two materials. The other variables in (13) follow Table 1.

Using Eq. (1), it shows that ΔT actually generates a local thermal bending moment τ_{thermal} to the cantilever as

$$\tau_{\mathrm{thermal}} = (E_1I_{1c} + E_2I_{2c})C\,\Delta T = K_{\mathrm{thermal}}\,\Delta T \tag{14}$$

The constant K_{thermal} represent the thermal bending moment coefficient of the BMC.

We put the thermal bending effect into the model. Firstly, we describe the temperature rise at linkage i by substituting τ_{thermal} and ΔT in Eq. (14) with $\tau_{\mathrm{thermal},i}$ and ΔT_i, respectively. Secondly, we described $\tau_{\mathrm{thermal},i}$ ($=K_{\mathrm{thermal}}\,\Delta T_i$) as a torque at linkage i by substituting $\vec{F}_i$ in Eq. (12) with $\tau_{\mathrm{thermal},i}$. Finally, the movement $\vec{q}_i$ resulted from $\tau_{\mathrm{thermal},i}$ becomes

$$\vec{q}_i = \theta_i - \theta_{i-1} \tag{15}$$

and Eq. (12) becomes

$$\frac{\mathrm{d}}{\mathrm{d}t}\left(\frac{\partial L}{\partial \dot{\theta}_k}\right) - \frac{\partial L}{\partial \theta_k} = K_{\mathrm{thermal}}(\Delta T_{k+1} - \Delta T_k),$$
$$k = 2, 3, \ldots, N-1 \tag{16}$$

The right-hand side of Eq. (16) becomes $K_{\mathrm{thermal}}(-\Delta T_N)$ when $k = N$.

3.1.3. The effect of air dragging

In addition to thermal bending moments, we also considered the non-conservative force provided by air dragging [17]. Again, referring to (12), for rod number i, the dragging force $\vec{F}_i$ and the corresponding displacement $\vec{q}_i$ are

$$\vec{F}_i = \tfrac{1}{2} b \rho_{\mathrm{a}} C_{\mathrm{d}} (\dot{\vec{P}}_i \cdot \hat{n}_i)^2 \hat{n}_i \cdot l \tag{17}$$

and

$$\vec{q}_i = \vec{P}_i \tag{18}$$

where $\hat{n}_i$ is a normal vector perpendicular to the rod, $\vec{P}_i$ the central position of rod i, ρ_{a} the density of air, and C_{d} the air dragging coefficient [17]. Since the Reynolds number Re is small for the micro-cantilever beam ($\ll$2300), the airflow crossing the micro-cantilever was laminar [17]. Therefore, $C_{\mathrm{d}} = K_{\mathrm{d}}/Re_{\mathrm{b}}$, where $Re_{\mathrm{b}} = \rho_{\mathrm{a}}(\dot{\vec{P}}_i \cdot \hat{n}_i)b/\mu$, K_{d} is a geometric constant ranging from 10 to 100 for the BMC in this work [17], and μ the absolute viscosity of air.

We combined the effects of thermal bending moments and air dragging and derived the comprehensive dynamics equations for the rods-and-linkages model. The equations could be represented in a matrix form

$$\begin{bmatrix} A_{1,1} & A_{1,2} & \cdots & A_{1,N} \\ A_{2,1} & A_{2,2} & & \vdots \\ \vdots & & \ddots & \vdots \\ A_{N,1} & \cdots & \cdots & A_{N,N} \end{bmatrix} \begin{bmatrix} \ddot{\theta}_1 \\ \ddot{\theta}_2 \\ \vdots \\ \ddot{\theta}_N \end{bmatrix} = \begin{bmatrix} B_1 \\ B_2 \\ \vdots \\ B_N \end{bmatrix} + \begin{bmatrix} \mathrm{QT}_1 \\ \mathrm{QT}_2 \\ \vdots \\ \mathrm{QT}_N \end{bmatrix} + \begin{bmatrix} \mathrm{QD}_1 \\ \mathrm{QD}_2 \\ \vdots \\ \mathrm{QD}_N \end{bmatrix} \tag{19}$$

where $A_{i,j}$ and B_i are the same as the ones in (9). QT_i and QD_i represent the effect of thermal bending moment and air dragging, respectively, and they are both functions of $\{\theta_k\}$ and $\{\dot{\theta}_k\}$.

3.2. Heat transfer model

Heat transfer in laser-heated BMC includes absorption of laser energy by the top layer, heat conduction from the top layer to the bottom layer, and heat conduction from the BMC to the base of the cantilever and the environment. Since the BMC in our experiment is so thin (0.5 μm for the Au layer and 1.5 μm for the poly-Si layer) and highly thermal-conductive,

we used a fin-model [18] to approach the heat transfer problem in the BMC. In this model, the cantilever length is L, the initial temperature of the BMC is a uniform temperature T_0, the clamped-end of the substrate part was set to be constant at T_0, and the free-end of the BMC is isolated. The transient heat conduction model follows:

$$(a_1\rho_1C_{V1} + a_2\rho_2C_{V2})\frac{\partial T(x,t)}{\partial t} = (a_1k_1 + a_2k_2)\frac{\partial^2 T(x,t)}{\partial x^2} + (1-R)I_{\text{in}}(x,t)\sin(\gamma) \quad (20)$$

where T is the temperature at position x and time t, R the reflectivity of the top surface, γ the laser's incident angle, and I_{in} the flux of laser energy applied to the top surface at position x and time t. The other coefficients in Eq. (20) follow Table 1. Eq. (20) will yield the temperature of the BMC as [14]

$$T(x,t) = T_0 + \sum_{n=1}^{\infty}\left[\int_0^t F_{\text{in},n}(\tau)\sin(\gamma)\,\mathrm{e}^{-\lambda_n^2\alpha^2(t-\tau)}\,\mathrm{d}\tau\right] \times\sin(\lambda_n x) \quad (21)$$

where

$$\alpha = \sqrt{\frac{k_1a_1 + k_2a_2}{a_1\rho_1C_{V1} + a_2\rho_2C_{V2}}},$$

$$F_{\text{in},n}(\tau) = \frac{2}{L}\int_0^L \frac{I_{\text{in}}(x,\tau)}{a_1\rho_1C_{V1} + a_2\rho_2C_{V2}}\sin(\lambda_n x)\,\mathrm{d}x$$

and $\lambda_n = (2n-1)\pi/2L$.

For example, in the case of the 850 μm BMC heated by one laser pulse (laser energy: 0.057 J/cm^2 per pulse; pulse width: 12 ns), the variation of temperature is calculated according to Eq. (21) and is shown in Fig. 8.

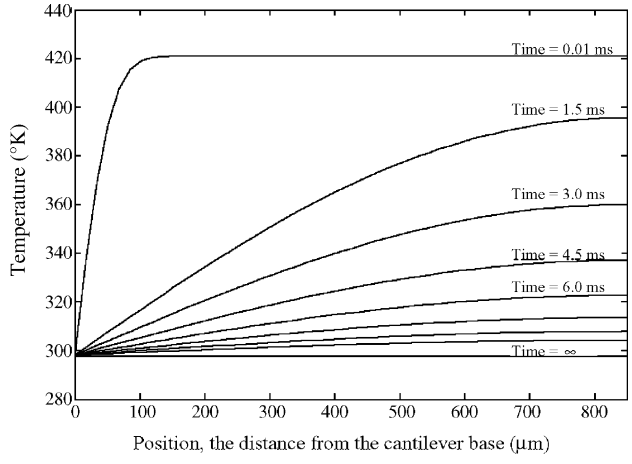

Fig. 8. The time-variant temperature distribution of an 850 μm BMC heated by a laser pulse (laser energy: 0.057 J/cm^2 per pulse; pulse width: 12 ns) is simulated with Eq. (21). Each curve represents the temperature distribution over the length of the BMC, and different curves represent the temperature distribution at a different time after the laser pulse is fired.

3.3. Simulation procedure

In our simulation, the initial conditions were: $T(x, 0) = 25\,^\circ$C, $\dot{\theta}_k(0) = 0$, and $\theta_{k+1}(0) - \theta_k(0) = \theta_{\text{equi}}|_{T=T_{\text{room}}}/N$. Here $\theta_{\text{equi}}|_{T=T_{\text{room}}}$ is the initial bending angle of the BMC generated by the temperature change $T_0 - T_{\text{fab}}$ from its fabrication temperature T_{fab}. We adjusted T_{fab} to fit the real BMCs. For the boundary conditions, the temperature at the clamped-end of the fin-model remained at T_0 and the thermal conduction at the BMC end of the fin-model was adiabatic, i.e. $(\partial T(x, t)/\partial x)|_{x=0} = 0$.

For I_{in}, we assumed that the laser power was uniform over the entire cantilever since the laser beam size was much larger than the BMC. We used a step-function to simulate the laser energy, and the laser energy was non-zero only within the interval from $t = 0$ to t_{w} (the laser pulse width). In each simulation cycle, we calculated the temperature at the position of each linkage ($x = 0, l, 2l, \ldots, Nl$) by using Eq. (21). These temperatures were then applied to Eq. (19) to obtain $\theta_k(t)$. According to Fig. 4, results of $\theta_k(t)$ were converted into the distance d as follows:

$$d \cong d_0 + l\sum_{k=1}^{N}\sin(\beta - \theta_k) \quad (22)$$

The geometric coefficients follow those of the BMCs in our experiment. Material characteristic coefficients, as listed in Table 1, were from Ref. [19].

4. Results and discussions

BMCs with lengths of 1000, 850, and 500 μm, were heated by a single pulse of 355 nm laser of different energies. The BMC response was measured by using the displacement sensor to detect the movement of the BMC tip. During the experiment, we analyzed the signal noises (from electronics, airflow, or mechanical vibrations other than BMC vibrations) and found that the frequencies and amplitudes of the noises did not cover at least the first order (and second order for 1000 and 850 μm BMCs, which have lower vibration frequencies) BMC vibration signals.

In Fig. 9 we show the experimental (solid curves) and simulated (dotted curves) responses of 1000, 850, and 500 μm BMCs heated by a single laser pulse of diameter 1 mm and powers of 84.4, 65.8, and 72.7 μJ/pulse. The vertical axis in each figure shows the distance d that we used in Fig. 4. Note that, an increase in the d means that the BMC is bending away from the DLD sensor and vice versa. The curves in Fig. 9a–c show that the BMCs vibrated after the delivery of the laser pulse. In both the experimental and simulated curves, we found that the centers between the local maximum and minimum experience a shifting during the vibration. Beyond a settling times t_{ss}, the shifting vanished. According to our model for temperature $T(x, t)$, we found that t_{ss} is about the time for the temperature of the cantilevers to recover to

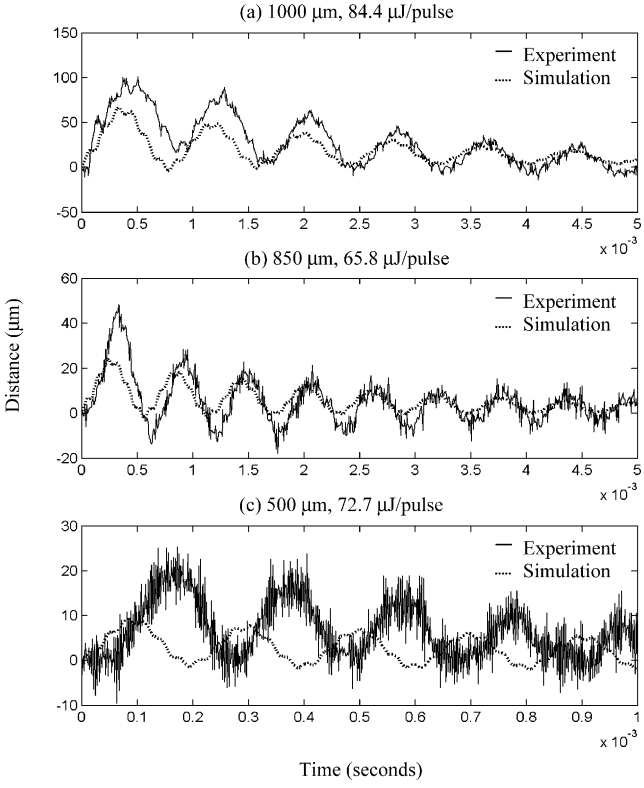

Fig. 9. The experimental and simulated displacements of the tips on the BMCs shoot by single laser pulses. The BMCs were of different lengths: 1000 μm (a), 850 μm (b), and 500 μm (c). The diameter of the laser beam was fixed to be 1 mm, while the laser powers for each case were different. The parameters in the simulations follow the specific laser energy and BMC length.

its initial temperature. On the other hand, our experimental result shows that the shifting is substantially proportional to the laser power. We believe that these shiftings were resulted from the heating and cooling processes in the BMCs, during which the equilibrium bending angles θ_{equi} decreased suddenly (or d increased suddenly) when the cantilevers was heated by the laser pulse, and it recovered gradually during cooling.

In addition to the center-shifting, the maximum displacement of the BMC tip is also substantially proportional to the laser energy. Fig. 10 shows the simulation and experimental results of maximum displacements of the BMCs of 1000, 850, and 500 μm long. These results suggest that increasing of the laser energy can significantly enlarge the displacement of the BMCs. The difference between slopes of the experimental and simulated data is likely due to modeling errors from material parameters, like approximation of the BMC surface reflectivity and thermal expansion coefficients of the BMC materials.

Note that damping effect was also considered in our model. We assumed that the damping is generated by air dragging only and is determined by the non-dimensional coefficient K_d, which was expected to be in the range between 10 and 100. In Fig. 9, K_d was selected to fit the

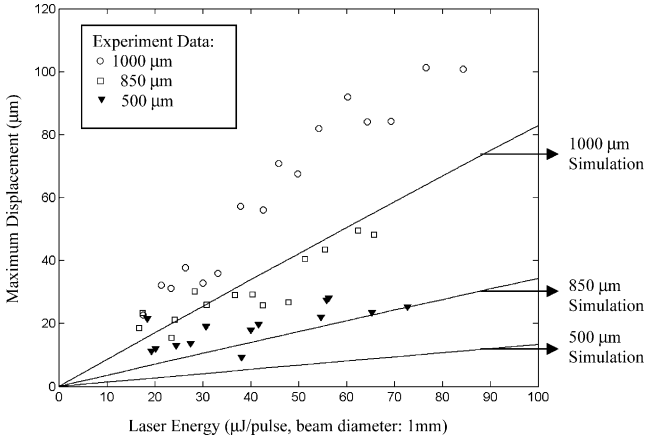

Fig. 10. The effect of laser power to the maximum displacement of the BMC tips.

decay tendencies of the experimental results, and the value was found to be about 60, which is within the range that we expected. Because K_d is theoretically independent to the properties of fluids [17], this could allow our model to predict the response of laser actuation of a BMC placed in liquids.

The accuracy of the simulation was further investigated by frequency spectrum analysis as shown in Fig. 11. The spectrums were derived by using fast Fourier transforms

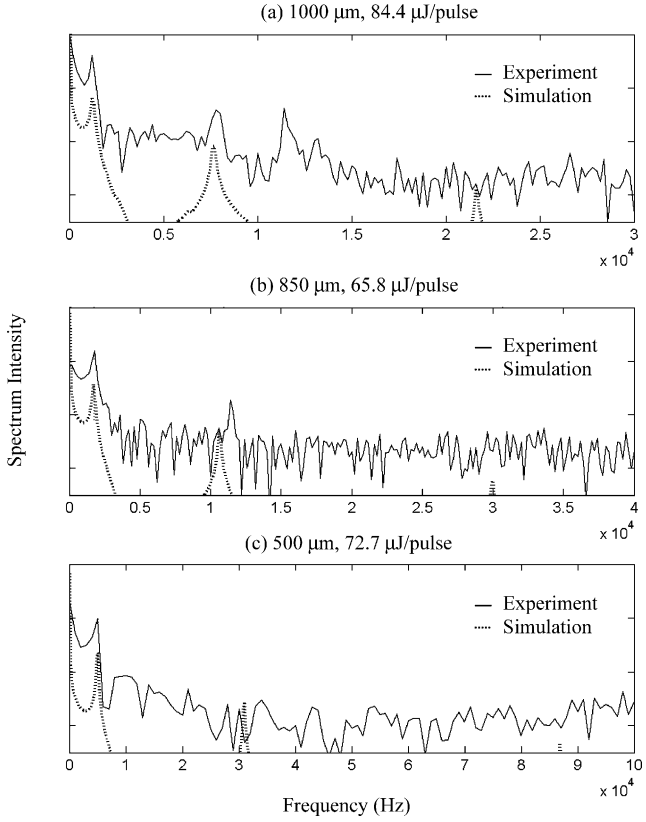

Fig. 11. Experimental (solid curve) and simulated (dotted curve) frequency spectrums.

[14], and the peaks on the spectrum curves could be used to indicate the vibration frequencies of the BMCs. For example, Fig. 11a shows the experimental spectrum of the 1000 μm BMC. These peaks indicate the first- and second-order vibrations [15] of the 1000 tm beam under pulsed laser heating. Because of the limit by bandwidth of the displacement sensor (20 kHz), vibration frequencies higher than 10 kHz were not identified. Similarly, Fig. 11b and c shows the vibration spectrums for BMCs of the 850 and 500 μm long. It is seen that the simulation results fit very well with the peaks of the experimental spectrums.

5. Conclusion

We have demonstrated wireless actuation of a BMC using pulsed laser heating. An experiment was developed to measure BMC vibrations using a displacement sensor. A 2D discrete model was built to simulate the process of laser-actuated BMC motion. Both the experimental results and numerical simulation revealed that the BMC responded by vibrations at the resonance frequency and significant shifting of the equilibrium position due to heat transfer from the laser to the BMC and finally to the substrate. From experimental data and the simulations discussed above, we have evidently shown that the pulse laser can effectively generate large movement in bimorph cantilevers. In the experiment using 1000 μm BMC, with the power of 84.4 μJ per pulse (laser diameter = 1 mm) one could generate a maximum displacement higher than 100 μm. This experiment has brought out the information about the feasibility and potential of using pulse laser heating in developing wireless micro-electro-mechanical systems. We believe that this finding could be utilized in the remote actuation of micro-pumps or micro-propellers.

Acknowledgements

This work was supported by a CAREER award (DMI 0222014) to SC from the US National Science Foundation. The SEM analysis was conducted in the Texas Materials Institute at the University of Texas at Austin. LH thanks Mr. Dongbing Shao and Dr. Shifeng Li for their help to this project.

References

[1] A. Camposeo, N. Puccini, F. Fuso, M. Allegrini, E. Arimondo, A. Tuissi, Laser deposition of shape-memory alloy for MEMS applications, Appl. Surf. Sci. 208–209 (2003) 518–521.
[2] C. Sones, S. Mailis, V. Apostolopoulos, I.E. Barry, C. Gawith, P.G.R. Smith, R.W. Eason, Fabrication of piezoelectric micro-cantilevers in domain-engineered $LiNbO_3$ single crystals, J. Micromech. Microeng. 12 (2002) 53–57.
[3] S. Zhou, X. Sun, W.N. Carr, A monolithic variable inductor network using microrelays with combined thermal and electrostatic actuation, J. Micromech. Microeng. 9 (1999) 45–50.
[4] C.A. Savran, A.W. Sparks, J. Sihler, J. Li, W. Wu, D.E. Berlin, T.P. Burg, J. Fritz, M.A. Schmidt, S.R. Manalis, Fabrication and characterization of a micromechanical sensor for differential detection of nanoscale motions, J. Microelectromech. Syst. 11 (2002) 703–708.
[5] J. Choi, J. Yamaguchi, S. Morales, R. Horowitz, Y. Zhao, A. Majumdar, Design and control of a thermal stabilizing system for a MEMS optomechanical uncooled infrared imaging camera, Sens. Actuators A 104 (2003) 132–142.
[6] E.A. Wachter, T. Thundat, P.I. Oden, R.J. Warmack, P.G. Datskos, S.L. Sharp, Remote optical detection using microcantilevers, Rev. Sci. Instrum. 67 (1996) 3434–3439.
[7] J.M.Z. Ocampo, P.O. Vaccaro, T. Fleischmann, T. Wang, K. Kubota, T. Aida, T. Ohnishi, A. Sugimura, R. Izumoto, M. Hosoda, S. Nashima, Optical actuation of micromirrors fabricated by the micro-origami technique, Appl. Phys. Lett. 83 (2003) 3647–3649.
[8] S. Baglio, S. Castorina, L. Fortuna, N. Savalli, Modeling and design of novel photo-thermo-mechanical microactuators, Sens. Actuators A 101 (2002) 185–193.
[9] S. Chen, C.P. Grigoropoulos, H.K. Park, P. Kerstens, A.C. Tam, Photothermal displacement measurement of transient melting and surface deformation during pulsed laser heating, Appl. Phys. Lett. 73 (1998) 2093–2095.
[10] L.G. Shamanaeva, Thermooptical mechanism of sound generation by high-power laser radiation propagating in the atmosphere, Russ. Phys. J. 44 (2001) 1187–1196.
[11] W.D. Callister, Materials Science and Engineering: An Introduction, Wiley, New York, 2003.
[12] H. Goldstein, Classical Mechanics, Addison-Wesley, 1950, p. 347.
[13] D. Karnopp, D.L. Margolis, R.C. Rosenberg, System Dynamics—Modeling and Simulation of Mechanical System, Wiley, 2000, p. 124.
[14] P.V. O'Neil, Advanced Engineering Mathematics, Belmont, 3rd ed., 1991.
[15] J.H. Williams Jr., Fundamentals of Applied Dynamics, Wiley, 1996.
[16] S. Timoshenko, Analysis of bi-metallic thermostates, J. Opt. Soc. Am. 11 (1925) 233.
[17] R.W. Fox, A.T. McDonald, Introduction to Fluid Mechanics, Wiley, Canada, 1994, pp. 418–422.
[18] F.P. Incropera, D.P. De Witt, Fundamentals of Heat and Mass Transfer, Wiley, New York, 1990.
[19] MatWeb, http://www.matweb.com/.